eJSE International

Special Issue: Electronic Journal of Structural Engineering 14(1) 2015

Analysis of mode conversion and scattering of guided waves at cracks in isotropic beams using a time-domain spectral finite element method

S. He & C.T. Ng

School of Civil, Environmental and Mining Engineering,
The University of Adelaide, Adelaide, Australia

Email: alex.ng@adelaide.edu.au

ABSTRACT: Detecting damages in its early stage, and hence, to ensure the safety and reliability of structures is of vital important. Guided waves have been recognised as one of the promising damage detection techniques that are sensitive to small and different types of damages. The understanding of guided wave propagation and scattering phenomena at the damages is one of the fundamental elements to facilitate the development of this technique for damage characterisation. This paper presents a study of scattering characteristics and mode conversion effects of guided waves at cracks in isotropic beams. An efficient time-domain spectral finite element method using one-dimensional (1D) beam element is developed to solve this problem. The developed model is then used to carry out a series of case studies that consider different crack sizes in the beams. These parametric studies provide a fundamental physical insight into the mode conversion phenomena and scattering characteristics of the guided waves at the cracks.

Keywords: Damage Detection, Guided Waves, Spectral Finite Element, Mode Conversion, Scattering, Crack

1 INTRODUCTION

The monitoring and maintenance of structural serviceability have increasingly attracted public attention in civil, mechanical and aeronautic engineering industries due to economic and safety reasons. Structural health monitoring (SHM) is of vital importance as it continuously examines the structural integrity and offers the valuable information of damages and material deterioration. SHM requires damage detection techniques that inspect the performance of individual structural components and detect any damage in its early stage. In recent decades, different methods (Doebling et al., 1996; Doebling et al., 1998; Sohn et al., 2004; Carden and Fanning, 2004; Fan and Qiao, 2011) have been applied to detect and characterise damage for increasing the safety, durability and reliability of structures, and also minimising their maintenance cost.

Among these methods, guided wave based approach has been proven to be one of the promising techniques for damage detection (Rose, 1999, 2002; Raghavan and Cesnik, 2007; Ostachowicz and Radzieński, 2012). This approach is capable of detecting small damages with high efficiency and outstanding sensitivity. An understanding of guided wave propagation and scattering characteristics plays one of the important roles in the development of damage detection methods.

Guided wave can propagate in different types of structures, which are generally classified into one-dimensional (1D) waveguide, such as beam-like structure, and two-dimensional (2D) waveguide, such as plate-like structures (Ng, 2014). Analytical solutions of guided wave scattering at damages are difficult to obtain due to the difficulties in simulating its complicated propagation and scattering characteristics at the damages, especially for complex structures.

Numerical methods, such as finite element (FE) method (Moser et al., 1999; Hong et al., 2013; Veidt and Normandin, 2013), finite difference (FD) method (Chu and Chaudhuri, 1989; Xu et al., 2003) and boundary element (BE) method (Zhao and Rose, 2003) are suitable for solving wave propagation problems in various structural environments but they are computationally expensive. Other numerical methods, such as finite strip element (FSE) method (Liu, 2002; Bergamini and Biondini, 2004), which is developed based on low level of discretisation, has difficulty in obtaining proper strip stiffness and mass matrix. Local interaction simulation approach (LISA)

is impractical in constructing the distribution of the mass matrix (Delsanto et al., 1992; Delsanto et al., 1994; Delsanto et al., 1997). The fast Fourier transform (FFT) based spectral finite element (SFE) method (Ng et al., 2009; Deepak et al., 2012; Ajith and Gopalakrishnan, 2013) were reported to be computationally efficient but it is not capable in simulating the guided waves in complex structures. Specifically, this method assumes that one side of the modelled beam must be infinitely long, which is impracticable in real applications for monitoring civil and mechanical engineering structural components.

Among all the numerical methods, the time domain SFE method (Kudela et al., 2007; Kudela and Ostachowicz, 2009; Rucka et al., 2012; Li et al., 2012) is one of the computational efficient approaches and is suitable to simulate the guided wave propagation in geometrically complex structures. It combines the advantages of FE method and spectral method (Boyd, 2001). The SFE method has the same flexibility of discretisation as FE method, thus, it can be easily implemented for analysis. Furthermore, the use of high order Gauss-Lobatto-Legendre (GLL) approximation polynomials leads to a diagonal mass matrix, and hence, the guided wave propagation simulation can be solved efficiently using the explicit central difference method. Also, in terms of simulating 1D guided wave propagation in beam-like structures, different wave propagation theories have been well developed for accounting dispersion effects of guided wave propagation. In this study, the Mindlin–Herrmann rod and Timoshenko beam theories are considered in the 1D SFE model for accounting lateral contraction, rotating mass inertia and shear deformation, respectively.

Admittedly, the surface cracks are the most commonly observed defects in many beam-like components, which are asymmetrically located along the structural depth direction. The mode conversion effect of guided waves occurs when the waves interacting with these non-axisymmetric discontinuities. This phenomenon has been investigated by a number of studies (Lowe et al., 2002; Castaings et al., 2002; Shkerdin and Glorieux, 2004; Benmeddour et al., 2008). Understanding this behaviour is of significant importance because it provides more information for further improving the performance of damage identification. Generally, the studies of the mode conversion effect focus on 2D waveguides, which usually use 3D or 2D structural models (Benmeddour et al., 2008; Zhou and Ichchou, 2011; Zhou et al., 2013; Xu et al., 2014) but it is computational expensive. In order to solve this problem, a 1D spectral cracked beam element is developed using Paris' equation (Tada et al., 2000) to study the mode conversion effect and scattering of guided waves at a semi-elliptical surface cracks. Different to most of 1D crack model, the crack in this SFE model is not across the full width of the beam.

The aims of this paper are to determine the scattering characteristics of guided waves at the cracks in the isotropic beam with rectangular cross section using 1D SFE method. It is worth mentioned that this method can be easily extended to 2D and 3D simulations. The 1D spectral crack element is proposed to couple the longitudinal, shear and bending displacements, and hence, enabling the prediction of mode conversion effects. Different locations, depths and widths of the surface cracks are considered in this study. In addition, the validity of the 1D SFE model will be verified using results calculated by 3D explicit FE model.

The organisation of this paper is presented as follow. The simulation of guided wave propagation using the proposed SFE method and the formulation of the SFE crack element are first described in Section 2. In Section 3, the verification of the SFE model using commercial FE software, ABAQUS, is presented and the mode conversion effect is then discussed in detail. After that, a parametric study is conducted to study the scattering characteristics of guided waves at the cracks in Section 4. Finally conclusions are drawn in Section 5.

2 TIME DOMAIN SPECTRAL FINITE ELEMENT METHOD

Guided wave propagation in structures can be expressed using the dynamic equilibrium equation as (Reddy, 2006)

$$\mathbf{M}\ddot{\mathbf{Q}} + \mathbf{C}\dot{\mathbf{Q}} + \mathbf{K}\mathbf{Q} = \mathbf{F} \tag{1}$$

where $\mathbf{M}$, $\mathbf{C}$ and $\mathbf{K}$ are the global mass matrix, damping matrix and stiffness matrix, respectively. $\mathbf{F}$ is the time domain excitation force vector. It is assumed that the global damping matrix $\mathbf{C}$ is proportional to the mass matrix as $\mathbf{C} = \eta\mathbf{M}$, and η is the damping coefficient. $\mathbf{Q}$, $\dot{\mathbf{Q}}$ and $\ddot{\mathbf{Q}}$ are the displacement, velocity and acceleration vectors, respectively.

In equation (1), the global mass matrix $\mathbf{M}$, stiffness matrix $\mathbf{K}$ and force vector $\mathbf{F}$ are determined by assembling the element matrix $\mathbf{M}^e$, $\mathbf{K}^e$ and $\mathbf{F}^e$. The expressions are similar to the conventional FE method (Reddy, 2006) and are defined as

$$\mathbf{M}^e \approx \sum_{i=1}^{n} w_i \mathbf{N}(\xi_i)^T \boldsymbol{\mu} \mathbf{N}(\xi_i) detJ(\xi_i) \quad (2)$$

$$\mathbf{K}^e \approx \sum_{i=1}^{n} w_i \mathbf{B}(\xi_i)^T \mathbf{D} \mathbf{B}(\xi_i) detJ(\xi_i) \quad (3)$$

$$\mathbf{F}^e \approx \sum_{i=1}^{n} w_i \mathbf{N}(\xi_i)^T \mathbf{p}(\xi_i) detJ(\xi_i) \quad (4)$$

where $\boldsymbol{\mu}$, $\mathbf{D}$ and $\mathbf{p}(\xi_i)$ are the mass density matrix, stress-strain matrix and external force vector, respectively. $\mathbf{N}(\xi_i)$ is the spectral shape function, $\mathbf{B}(\xi_i)$ is the strain-displacement operator and J is the Jacobian functions mapping the element nodes from local domain to global domain, which are expressed in a general form as

$$\mathbf{N}_i(\xi) = \prod_{m=1, m\neq i}^{n} \frac{\xi - \xi_m}{\xi_i - \xi_m}, \quad i(i \in 1,2,...,n) \quad (5)$$

$$\mathbf{B}(\xi) = \mathbf{L}\mathbf{N}_i(\xi), \quad and \quad J = \frac{\partial x}{\partial \xi} \quad (6)$$

where n is the number of total integrated nodes and m is the order of node considered. $\mathbf{L}$ is the differential operator based on wave propagation theories and its formula is given in Section 2.2. The abscissas ξ_i of each integrated GLL node are shown in Figure 1, which can be obtained by calculating the roots of the following equation (Pozrikidis, 2005)

$$(1-\xi^2) P'_{n-1}(\xi) = 0, \quad \xi_i \in [-1,1] \quad (7)$$

where P'_{n-1} is the first derivative of the $(n\text{-}1)^{\text{th}}$ order of Legendre polynomial. The weights w_i corresponding to the abscissa ξ_i can be calculated from the following equation (Pozrikidis, 2005)

$$w_i = \frac{2}{n(n-1)[P_{n-1}(\xi_i)]^2} \quad (8)$$

Applying this GLL integration, the spectral shape function has the following properties (Ostachowicz et al., 2012)

$$\mathbf{N}_j(\xi_i) = \delta_{ji}, \quad j(j \in 1,2,...,n) \quad \text{and} \quad \sum_{j=1}^{n} \mathbf{N}_j(\xi_i) = 1 \quad (9)$$

where δ_{ji} is the Kroneker delta. As shown in Figure 2 (Kudela et al., 2007), the spectral shape function is orthogonal, and hence, a diagonal local mass matrix $\mathbf{M}^e$ can be obtained using this spectral shape function. As a result, the explicit time integration scheme, i.e. central difference method (Ostachowicz et al., 2012) can be used to solve the dynamic equation (1) efficiently. Furthermore, the Runge effect is avoided by the application of this GLL-node element (Pozrikidis, 2005).

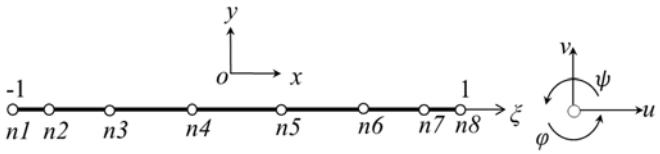

Figure 1. Distribution of GLL nodes and the degrees-of freedom at each node

Based on the aforementioned equations, the SFE model for wave propagation in beams can be developed based on the Mindlin-Herrmann rod and Timoshenko beam theory.

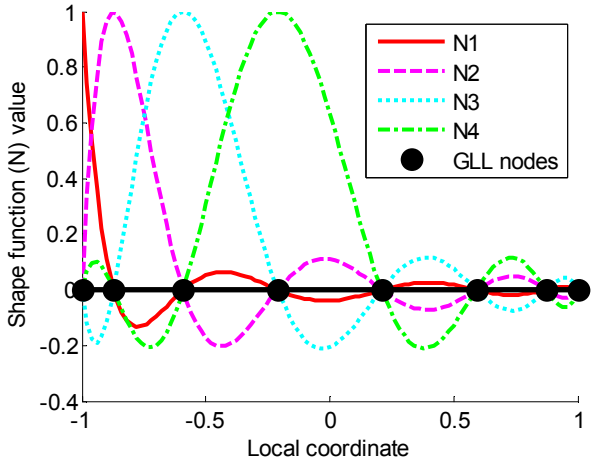

Figure 2. First four 8-node element's shape functions

2.1 Mindlin-Herrmann and Timoshenko beam theory

The Mindlin-Herrmann rod theory is used to simulate the longitudinal wave propagation in the proposed model, while Timoshenko beam theory is employed to simulate the flexural wave propagation. The Mindlin-Herrmann rod theory introduces the independent lateral contraction $\psi(x)$ to approximate the Poisson effect (Mindlin and Herrmann, 1951) due to the longitudinal wave propagation, while the Timoshenko beam theory considers the effect of shear deformation and introduces the independent rotation $\varphi(x)$ as shown in Figure 1. The beam element has n nodal points, in which each nodal point has four DoFs. The displacement field can be expressed as

$$\bar{u}(x,y) \approx u(x) - y\varphi(x)$$

$$\bar{v}(x,y) \approx \psi(x) y + v(x) \quad (10)$$

where $v(x)$ is the independent vertical displacement introduced based on the Timoshenko beam

theory, $u(x)$ is the longitudinal displacement by Mindlin-Herrmann rod theory and y is the vertical distance from neutral axis.

The governing equations for Mindlin-Herrmann rod theory are defined as (Doyle, 1989)

$$\frac{2GA}{1-\upsilon}\left(\frac{\partial^2 u}{\partial x^2}+\upsilon\frac{\partial \psi}{\partial x}\right)=\rho A\ddot{u}-p(x,t),$$

$$K_1^M GI\frac{\partial^2 \psi}{\partial x^2}-\frac{2GA}{1-\upsilon}\left(\upsilon\frac{\partial \psi}{\partial x}+\psi\right)=K_2^M\rho I\ddot{\psi} \tag{11}$$

where E, G, A, υ, ρ and I denote the Young's modulus, shear modulus, cross-section area, Poisson's ratio, mass density and moment of inertia, respectively. $p(x,t)$ is the longitudinal excitation, and t and x are its temporal and spatial variables, respectively.

The kinetic energy T_M and the strain energy U_M for Mindlin-Herrmann rod theory can be expressed as

$$\begin{aligned}T_M&=\frac{1}{2}\int_L(\rho A\dot{u}^2+K_2^M\rho I\dot{\psi}^2)\,dx,\\ U_M&=\frac{1}{2}\int_L\left\{\frac{EA}{1-\upsilon^2}\left[\left(\frac{\partial u}{\partial \mathrm{x}}\right)^2+\psi^2+2\upsilon\frac{\partial u}{\partial \mathrm{x}}\psi\right]\right.\\ &\qquad\left.+K_1^M GI\left(\frac{\partial \psi}{\partial \mathrm{x}}\right)^2\right\}dx\end{aligned} \tag{12}$$

The governing equations for Timoshenko beam theory are defined as (Doyle, 1989)

$$K_1^T GA\frac{\partial}{\partial x}\left(\frac{\partial v}{\partial x}-\varphi\right)=\rho A\ddot{v}-f(x,t),$$

$$I\frac{\partial^2 \varphi}{\partial x^2}-K_1^T GA\left(\frac{\partial v}{\partial \mathrm{x}}-\varphi\right)=K_2^T\rho I\ddot{\varphi} \tag{13}$$

where $f(x,t)$ is the transverse excitation.

The kinetic energy T_T and the strain energy U_T for Timoshenko beam theory can be expressed as

$$\begin{aligned}T_T&=\frac{1}{2}\int_L(\rho A\dot{v}^2+K_2^T\rho I\dot{\varphi}^2)\,dx,\\ U_T&=\frac{1}{2}\int_L\left\{EI\left(\frac{\partial \varphi}{\partial \mathrm{x}}\right)^2+K_1^T GA\left(\frac{\partial v}{\partial \mathrm{x}}-\varphi\right)^2\right\}dx\end{aligned} \tag{14}$$

where K_1^M, K_2^M, K_1^T, and K_2^T are adjustable variables that influence the group velocity of wave propagation and they can be determined experimentally (Doyle, 1989).

2.2 Spectral element modelling

Considering the Mindlin-Herrmann rod theory and Timoshenko beam theory, the strains can be represented in the following form (Rucka, 2010)

$$\boldsymbol{\varepsilon}=\begin{Bmatrix}\boldsymbol{\varepsilon}^M\\ \boldsymbol{\varepsilon}^T\end{Bmatrix}=\begin{Bmatrix}\mathbf{L}^M & 0\\ 0 & \mathbf{L}^T\end{Bmatrix}\begin{Bmatrix}\mathbf{u}^M\\ \mathbf{v}^T\end{Bmatrix} \tag{15}$$

where the superscripts M and T denote the Mindlin-Herrmann rod theory and Timoshenko beam theory, respectively. The total strain consists of $\boldsymbol{\varepsilon}^M$ and $\boldsymbol{\varepsilon}^T$, which have the following forms

$$\boldsymbol{\varepsilon}^M=\begin{bmatrix}\frac{\partial u}{\partial x}\\ \psi\\ \frac{\partial \psi}{\partial \mathrm{x}}\end{bmatrix}\quad\text{and}\quad\boldsymbol{\varepsilon}^T=\begin{bmatrix}\frac{\partial v}{\partial x}-\varphi\\ \frac{\partial \varphi}{\partial x}\end{bmatrix} \tag{16}$$

$\mathbf{L}^M$ and $\mathbf{L}^T$ are the differential operators, and $\mathbf{u}^M$ and $\mathbf{u}^T$ are displacements, they are denoted as

$$\mathbf{L}^M=\begin{bmatrix}\frac{\partial}{\partial x} & 0\\ 0 & 1\\ 0 & \frac{\partial}{\partial x}\end{bmatrix}=\begin{bmatrix}\frac{1}{J}\frac{\partial}{\partial \xi} & 0\\ 0 & 1\\ 0 & \frac{1}{J}\frac{\partial}{\partial \xi}\end{bmatrix},$$

$$\mathbf{L}^T=\begin{bmatrix}\frac{\partial}{\partial x} & -1\\ 0 & \frac{\partial}{\partial x}\end{bmatrix}=\begin{bmatrix}\frac{1}{J}\frac{\partial}{\partial \xi} & -1\\ 0 & \frac{1}{J}\frac{\partial}{\partial \xi}\end{bmatrix}, \tag{17}$$

$$\mathbf{u}^M=\begin{bmatrix}u\\ \psi\end{bmatrix},\quad\mathbf{u}^T=\begin{bmatrix}v\\ \varphi\end{bmatrix} \tag{18}$$

The mass density matrix $\boldsymbol{\mu}$ in equation (2) and the stress-strain matrix $\mathbf{D}$ in equation (3) are denoted as below

$$\mathbf{D}=\begin{Bmatrix}\mathbf{D}^M & 0\\ 0 & \mathbf{D}^T\end{Bmatrix},\quad\boldsymbol{\mu}=\begin{Bmatrix}\boldsymbol{\mu}^M & 0\\ 0 & \boldsymbol{\mu}^T\end{Bmatrix} \tag{19}$$

where

$$\mathbf{D}^M=\begin{bmatrix}\frac{EA}{1-\upsilon^2} & \frac{\upsilon EA}{1-\upsilon^2} & 0\\ \frac{\upsilon EA}{1-\upsilon^2} & \frac{EA}{1-\upsilon^2} & 0\\ 0 & 0 & K_1^M GI\end{bmatrix},$$

$$\mathbf{D}^T = \begin{bmatrix} K_1^T GA & 0 \\ 0 & EI \end{bmatrix}, \tag{20}$$

and

$$\boldsymbol{\mu}^M = \begin{bmatrix} \rho A & 0 \\ 0 & K_2^M \rho I \end{bmatrix}, \ \boldsymbol{\mu}^T = \begin{bmatrix} \rho A & 0 \\ 0 & K_2^T \rho I \end{bmatrix} \tag{21}$$

Based on the number of DoFs considered, the spectral shape function has the following expression

$$\mathbf{N}_i(\xi) = \begin{bmatrix} N_i(\xi) & 0 & 0 & 0 \\ 0 & N_i(\xi) & 0 & 0 \\ 0 & 0 & N_i(\xi) & 0 \\ 0 & 0 & 0 & N_i(\xi) \end{bmatrix} \tag{22}$$

The element mass matrix $\mathbf{M}^e$, stiffness matrix $\mathbf{K}^e$ and external force matrix $\mathbf{F}^e$ can be obtained by substituting equations (19), (20), (21) and (22) into (2), (3) and(4). The global matrices can be obtained by assembling the element matrices, and hence, the guided wave can be simulated by solving equation (1).

2.3 Crack element modelling

The crack element contains a single transverse opened crack, which is modelled using a two-node beam element with three DoFs per node, i.e. $u(x)$, $v(x)$, and $\varphi(x)$. There is no lateral contraction considered in this crack element so when the crack element is connected to the beam elements, the transmitted displacements $\psi(x)$ are assumed to be zero. This is because the lateral contraction caused by low frequency waveguide (e.g. 100 kHz) in the Mindlin-Herrmann rod theory is inconsequential compared with the rotation $\varphi(x)$ in the Timoshenko beam theory. Hence, there are totally six DoFs (i.e. $q_1, q_2, ..., q_6$) in this crack element as shown in Figure 3a. In order to account for the presence of the crack, the stiffness matrix has been modified similarly using the approach proposed by Darpe et al. (2004) with considering the coupled effects for three DoFs of each node, i.e., longitudinal, shear and rotation of displacements. It is assumed that the cross section of the beam is rectangle in this paper.

The geometry of the crack element is shown in Figure 3b. It has width (b), depth (h) and length (L_c), with a crack located at a distance x_c from the left end of the element having width b_c and depth d_c. In addition, each DoF at the first node of the crack element is assumed to be loaded with axial force P_1, shear force P_2 and bending moment P_3, respectively.

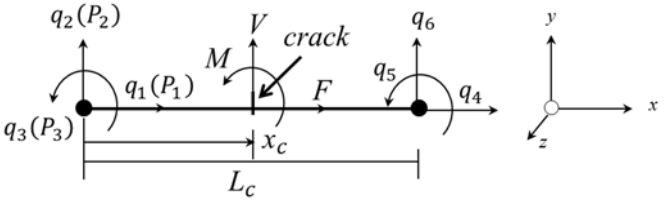

(a) Schematic diagram of the crack element

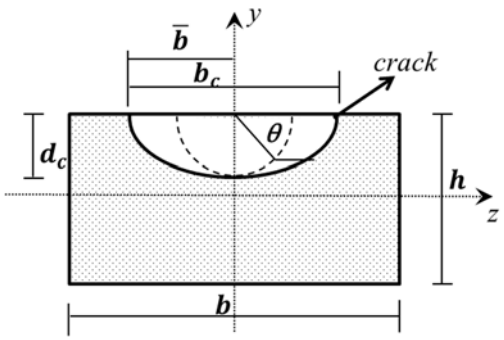

(b) Crack cross section

Figure 3. Dimensions, nodal displacement and forces details

In order to obtain the modified stiffness matrix for the SFE method, the flexibility matrix is first calculated using Castigliano's theorem

$$q_{ii} = \frac{\partial U}{\partial P_{ii}}, (ii \in 1,2,3) \tag{23}$$

where q_{ii} is the displacement of the first node corresponded to the *ii*th DoF. U is the total strain energy, which has the following form (Tada et al., 2000)

$$U = U^u + U^c \tag{24}$$

where U^u is the elastic strain energy for uncracked element while U^c is the strain energy caused by the crack. Thus equation (23) becomes

$$q_{ii} = q_{ii}^u + q_{ii}^c = \frac{\partial U^u}{\partial P_{ii}} + \frac{\partial U^c}{\partial P_{ii}} \tag{25}$$

where q_{ii}^u and q_{ii}^c are the displacement of uncracked beam and the additional displacement due to crack, respectively.

Considering the action of axial force *F*, shear force *V* and bending moment *M* at x_c (Figure 3a), the uncracked strain energy of the element can be expressed as

$$U^u = \frac{1}{2}\int \left[\frac{\alpha_s V^2}{GA} + \frac{F^2}{EA} + \frac{M^2}{EI} \right] dx \tag{26}$$

where $\alpha_s = 10(1+\upsilon)/(12+11\upsilon)$ is the shear coefficient for rectangular cross section (Cowper, 1966; Kawashima, 1996).

In equation (26), F, V and M have the following relationships with external nodal forces

$$F(x)=p_1,\ V(x)=p_2, \text{ and } M(x)=p_2x_c-p_3 \quad (27)$$

Thus equation (26) can be rewritten as

$$U^u=\frac{1}{2}\left[\frac{P_1^2L_c}{EA}+\frac{\alpha_s P_2^2L_c}{GA}+\frac{P_2L_c^3}{3EI}-\frac{P_2P_3L_c^2}{EI}+\frac{P_3^2L_c}{EA}\right] \quad (28)$$

Considering equation (23), the individual displacement of undamaged beam q_{ii}^u can be expressed as

$$q_1^u=\frac{\partial U^u}{\partial P_1}=\frac{P_1L}{EA},$$

$$q_2^u=\frac{\partial U^u}{\partial P_2}=\left(\frac{\alpha_sL}{GA}+\frac{L^3}{3EI}\right)P_2-\frac{L^2}{2EI}P_3 \ ,$$

$$q_3^u=\frac{\partial U^u}{\partial P_3}=\frac{L}{EA}P_3-\frac{L^2}{2EI}P_2 \quad (29)$$

Similarly, the additional displacement q_{ii}^c due to the crack can be obtained using the cracked strain energy from equation (23)

$$q_{ii}^c=\frac{\partial U^c}{\partial P_{ii}} \quad (30)$$

$$U^c=\int_A S(A)dA \quad (31)$$

where $S(A)$ is the strain energy density function and it is defined as

$$S(A)=\frac{1}{E'}\left[\left(\sum_{ii=1}^{3}K_{Iii}\right)^2+\left(\sum_{ii=1}^{3}K_{IIii}\right)^2\right] \quad (32)$$

where K_{Iii} and K_{IIii} are the stress intensity factors (SIFs) for the first and second mode of the crack displacement corresponding to q_{ii}. $E'=E$ for plane stress, and $E'=E/(1-\upsilon^2)$ for plane strain situation. The derivation of SIFs is written as follow.

SIFs for the first mode I (sliding)

$$K_{I1}=\sigma_1\sqrt{\frac{\pi d_c}{Q}}F_I$$

where $\sigma_1=\frac{P_1}{bh}$,

Thus $K_{I1}=\frac{P_1}{bh}\sqrt{\frac{\pi d_c}{Q}}F_I \quad (33)$

$$K_{I3}=\sigma_3H\sqrt{\frac{\pi d_c}{Q}}F_I$$

where $\sigma_3=\frac{6M_1}{bh^2}=\frac{6\left(P_2x_c-P_3\right)}{bh^2}$

Hence $K_{I3}=\frac{6\left(P_2x_c-P_3\right)}{bh^2}H\sqrt{\frac{\pi d_c}{Q}}F_I \quad (34)$

$K_{I2}=0$.

SIFs for the second mode II (tearing)

$$K_{II2}=\sigma_2\sqrt{\pi d_c}F_{II},$$

where $\sigma_2=\frac{\alpha_sP_2}{bh}$,

Hence $K_{II2}=\frac{\alpha_sP_2}{bh}\sqrt{\pi d_c}F_{II} \quad (35)$

where

$$Q=1+1.464\kappa^{1.65} \quad (36)$$

The function F_I (Newman Jr and Raju, 1981) and F_{II} (He and Hutchinson, 2000) are the boundary-calibration factors corresponding to tension and shear for $0<d_c/\bar{b}\le 1$, $0\le d_c/h<1$, $\bar{b}/b_c\le 0.5$ and $0\le\theta\le\pi$, which have the forms

$$F_I=\left[M_1+M_2\left(\frac{d_c}{h}\right)^2+M_3\left(\frac{d_c}{h}\right)^4\right]f_\theta g f_w \quad (37)$$

$$F_{II}=\frac{m(d_c/h)\cos\theta}{B\left[\sin^2\theta+(d_c/h)^2\cos^2\theta\right]^{1/4}} \quad (38)$$

where

$$M_1=1.13-0.09\kappa$$

$$M_2=-0.54+\frac{0.89}{0.2+\kappa}$$

$$M_3=-0.5-\frac{1.0}{0.65+\kappa}+14\left(1.0-\kappa\right)^{24} \quad (39)$$

$$g=1+\left[0.1+0.35\left(\frac{d_c}{h}\right)^2\right]\left(1-\sin\theta\right)^2 \quad (40)$$

The angular function f_θ for the half elliptical crack in function F_I is

$$f_\theta=\left[\kappa^2\cos^2\theta+\sin^2\theta\right]^{1/4} \quad (41)$$

The finite width calibrated function f_w is

$$f_w=\left[\sec\left(\frac{\pi b_c}{4b}\sqrt{\frac{d_c}{h}}\right)\right]^{1/2} \quad (42)$$

The product of H and F_I is the boundary-calibration factor for bending, where H is expressed

$$H = H_1 + (H_2 - H_1)(\sin\theta)^{(0.2+\kappa+0.6d_c/h)} \tag{43}$$

where

$$H_1 = 1 - 0.34\frac{d_c}{h} - 0.11\kappa\left(\frac{d_c}{h}\right)$$

$$H_2 = 1 - G_1\left(\frac{d_c}{h}\right) + G_2\left(\frac{d_c}{h}\right)^2 \tag{44}$$

where in H_2

$$G_1 = [1.22 + 0.12\kappa]$$

$$G_2 = \left[0.55 - 1.05\kappa^{0.75} + 0.47\kappa^{1.5}\right] \tag{45}$$

In function F_{II}

$$m = 1 - \kappa^2 \tag{46}$$

$$B = (m - \upsilon)E(m) + \upsilon\kappa^2 K(\mathrm{m}) \tag{47}$$

where the elliptic integrals are

$$E(m) = \int_0^{\pi/2}\sqrt{1 - m\sin^2\theta}\,d\theta$$

$$K(m) = \int_0^{\pi/2}\frac{d\theta}{\sqrt{1 - m\sin^2\theta}} \tag{48}$$

Substituting these SIFs into equations (31) and (32), equation (30) becomes

$$q_1^c = \left[P_1 I_{c1} + (xP_2 - P_3)I_{c2}\right]$$

$$q_2^c = \left[xP_1 I_{c2} + P_2 I_{c3} + (xP_2 - P_3)xI_{c4}\right]$$

$$q_3^c = \left[-P_1 I_{c2} - (xP_2 - P_3)I_{c4}\right] \tag{49}$$

where

$$I_{c1} = \frac{8\pi\kappa^2}{Eb^2h^2Q}\int_0^{\bar{b}}\int_0^{\pi/2}\bar{b}^2\sin^2\theta F_1^2\,d\theta d\bar{b},$$

$$I_{c2} = \frac{48\pi\kappa^2}{Eb^2h^3Q}\int_0^{\bar{b}}\int_0^{\pi/2}\bar{b}^2\sin^2\theta HF_1^2\,d\theta d\bar{b},$$

$$I_{c3} = \frac{8\alpha_s^2\pi\kappa^2}{Eb^2h^2}\int_0^{\bar{b}}\int_0^{\pi/2}\bar{b}^2\sin^2\theta F_{II}{}^2\,d\theta d\bar{b},$$

$$I_{c4} = \frac{288\pi\kappa^2}{Eb^2h^4Q}\int_0^{\bar{b}}\int_0^{\pi/2}\bar{b}^2\sin^2\theta H^2F_1^2\,d\theta d\bar{b},$$

$$\kappa = \frac{d_c}{\bar{b}}, \tag{50}$$

Hence, the total displacement q_k of the two-node spectral crack element can be expressed in a matrix form as

$$[q_k] = \mathbf{C}_{flex}[P_k] \qquad (k = 1,2,\ldots,6) \tag{51}$$

where $\mathbf{C}_{flex}$ is the flexibility matrix and it is defined as

$$\mathbf{C}_{flex} = \begin{pmatrix} c_{11} & c_{12} & c_{13} \\ c_{21} & c_{22} & c_{23} \\ c_{31} & c_{32} & c_{33} \end{pmatrix} \tag{52}$$

with

$$c_{11} = \frac{L_c}{EA} + I_{c1},$$

$$c_{22} = \left(\frac{\alpha_s L_c}{GA} + \frac{L_c^3}{3EA}\right) + \left(I_{c3} + x_c^2 I_{c4}\right),$$

$$c_{33} = \frac{L_c}{EI} + I_{c5},\quad c_{12} = c_{21} = x_c I_{c2},$$

$$c_{13} = c_{31} = -I_{c2},\quad c_{23} = c_{32} = -\frac{L_c^2}{2EA} - x_c I_{c4} \tag{53}$$

The stiffness matrix could be obtained using the transformation matrix $\mathbf{P}$ to consider the static equilibrium of the crack element.

$$\{q_1 \quad q_2 \quad q_3 \quad q_4 \quad q_5 \quad q_6\}^T = \mathbf{P}\{q_1 \quad q_2 \quad q_3\}^T \tag{54}$$

where the subscripts of q denote the orders of the DoFs of this two-node crack element, and the transformation matrix $\mathbf{P}$ is given by

$$\mathbf{P}^T = \begin{pmatrix} 1 & 0 & 0 & -1 & 0 & 0 \\ 0 & 1 & 0 & 0 & -1 & L_c \\ 0 & 0 & 1 & 0 & 0 & -1 \end{pmatrix} \tag{55}$$

The stiffness matrix of the spectral crack element is given as follow

$$\mathbf{K}^c = \mathbf{P}\mathbf{C}_{flex}^{-1}\mathbf{P}^T \tag{56}$$

Assembling the spectral crack element stiffness matrix $\mathbf{K}^c$ with other uncrack spectral element stiffness matrices $\mathbf{K}^e$, the global stiffness matrix $\mathbf{K}$ in equation (1) can be obtained, and hence, the axial-flexural coupling effect of the guided wave interaction with cracks is consider in the time domain SFE model.

3 MODEL VERIFICATION

3.1 Comparison of SFE and 3D FE results

The SFE model was verified using a 3D FE model in this section. The goal of this verification is to demonstrate 1) the accuracy of predicting guided wave propagation in the isotropic beam using SFE method and 2) the capability of the developed spectral crack element in simulating the guided wave scattering and mode conversion at the cracks.

An aluminium beam with length 1 m, width 0.012 m and depth 0.006 m was considered in the verification. The beam having a crack with width $b_c = 0.006$ m and depth $d_c = 0.003$ m located at $x = 0.25$ m of the beam is shown in Figure 5. It should be noted that the crack was modelled asymmetrically with regard to the depth direction of the beam. The Young's modulus E, density ρ and Poisson's ratio υ are 200×10^9 GPa, 7556 kgm^{-3} and 0.3, respectively. The excitation signal was a 100 kHz narrow-band six-cycle sinusoidal tone burst modulated by a Hanning window. It was applied as a nodal displacement in vertical direction at $x = 0$ m to excite the A_0 guided wave. The horizontal and vertical displacement responses were also measured at the same position (i.e. $x = 0$ m).

3.1.1 *Results calculated by SFE method*

The proposed SFE beam model was implemented using MATLAB. The beam was modelled using 40 SFEs, with eight GLL nodes in each element. The crack was modelled using the proposed spectral crack element. Damping was considered and it was assumed that the damping coefficient η is 550 s^{-1}. The central difference method was utilised to solve the dynamic equilibrium equation (1) and the time step Δt was 10^{-7} sec, which ensures the accuracy of the simulations. The simulated displacement response at $x = 0$ m is shown in Figure 4.

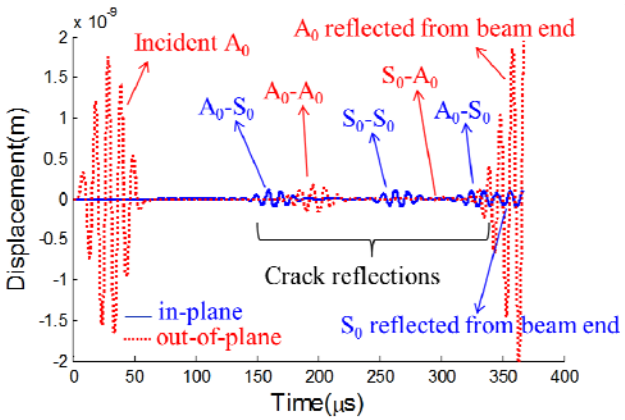

Figure 4. Displacement response measured at $x = 0$ m. (S_0: blue solid line; A_0: red dashed line)

The guided wave propagates along the length of the beam. When the incident A_0 guided wave first interacted with the crack located at the middle of the beam, the S_0 guided wave was generated due to the mode conversion effect. In Figure 4, the solid line shows the mode-converted S_0 guided waves. The first and third wave packs are the mode-converted S_0 guided waves from the crack. The second and fourth wave packs are these mode-converted S_0 guided waves reflected from the crack and the beam end at $x = 0.5$ m, respectively.

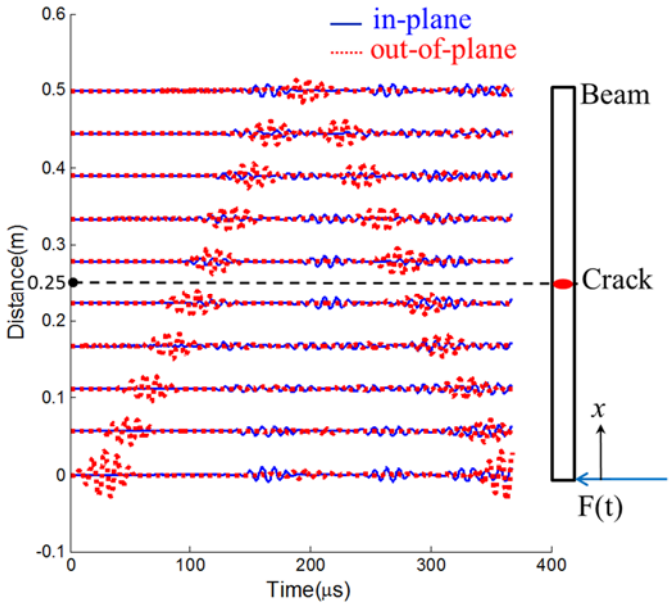

Figure 5. Guided wave propagation in the beam with a crack located at 0.5 m. (S_0: blue solid line; A_0: red dashed line)

The dashed line shows the A_0 guided waves. The first wave pack is the incident wave. The second wave pack is the A_0 guided wave reflected from the crack. The aforementioned mode-converted S_0 guided wave from the crack reflected from the beam end at $x = 0$ m and then propagated toward the crack. When the mode-converted S_0 guided wave interacted with the crack, it produced the mode-converted A_0 guided wave, which is the third wave pack of the dashed line in Figure 4. The last wave pack is the A_0 incident wave reflected from the beam end at $x = 0.5$ m. Figure 5 shows the details of the guided wave propagations along the beam and the mode conversions between A_0 and S_0 guided waves at the crack.

3.1.2 *Results calculated by 3D FE method and comparison*

A 3D FE model was constructed using the commercial software, ABAQUS, to verify the proposed SFE model. The FE beam geometry and the excitation signal were the same as the SFE model. The 3D explicit linear brick elements with 8 nodes per each element and three DoFs per node were used to model the beam. Because the amplitude of the guided wave was too small to cause large deformation, the geometrical nonlinear phenomena were not considered in verifying the SFE model. The 3D stress situation, full integration and the second-order accuracy of integration were considered in the model.

The crack was modelled using seam crack in the ABAQUS and the size of the crack was identical to that in the SFE model. A very small mesh size (i.e. approximately 0.4×0.4 mm^2) was chosen for meshing, and hence, 12 elements along the depth of the beam were generated as shown in Figure 6. This ensures the accuracy of simulating the 100 kHz A_0 and S_0 guided waves (Veidt and Ng, 2011; Ng and Veidt, 2011; Ng et al., 2012).

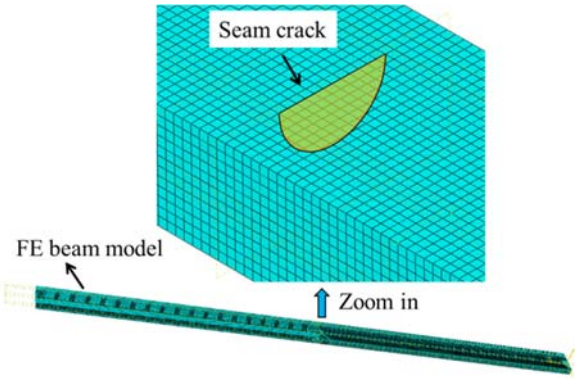

Figure 6. 3D FE mesh of the beam and the seam crack

A very good agreement was found between the FE and SFE results. A comparison between the A_0 guided waves calculated by the FE and SFE method is shown in Figure 7a, where the solid line represents the displacement response obtained from FE method and the dashed line was from the proposed SFE method. Figure 7a shows that the arrival time and the amplitudes of A_0 guided waves reflected from the crack and beam end at $x = 0.5$ m have a good agreement between the SFE and FE method. Figure 7b shows the results of the S_0 guided wave. A good agreement of the results between the FE and SFE method was found from the reflected S_0 guided waves. Figures 7a and 7b indicate that the proposed SFE model is able to simulate the guided wave propagation, scattering and mode conversion effect at the crack accurately.

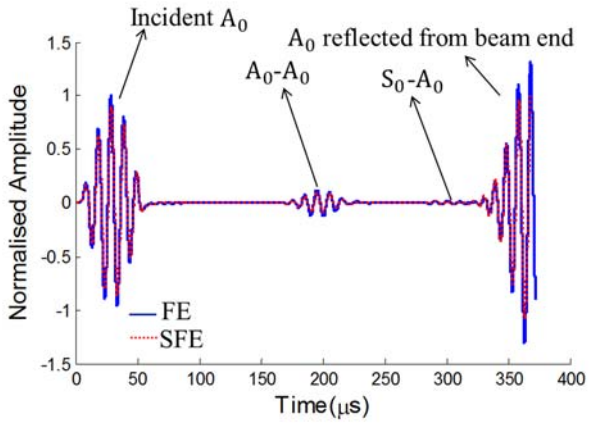

(a) Normalised displacement amplitude of A_0 guided wave

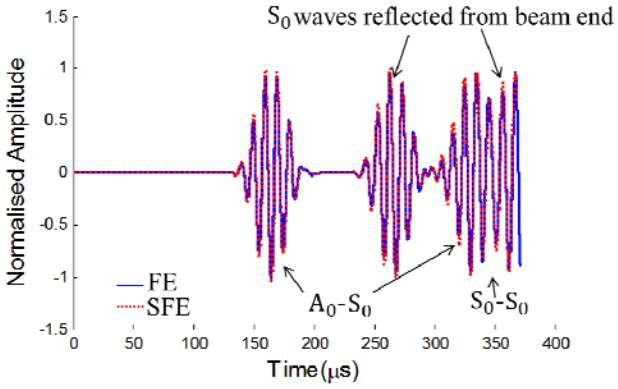

(b) Normalised displacement amplitude of S_0 guided wave

Figure 7. 3D-FE verification for the SFE model (FE results: blue solid line; SFE results: red dashed line)

3.2 Mode conversion effect

In engineering practice, the mode conversion is of great value for damage identification (Ramadas et al., 2010). Because different modes of guided waves have different properties, understanding the fundamental physics of this phenomenon plays an important role in developing damage detection techniques.

For example in a cantilever beam, cracks usually exist closed to the fixed end of the beam. Identification of these cracks using single guided wave mode is difficult as the A_0 guided wave reflection from the crack (e.g. A_0-A_0) is mixed with the A_0 guided wave reflected from the beam end as shown in Figure 8. However, the generation of the mode-converted S_0 guided wave signal (i.e. A_0-S_0) clearly reveals the existence of the cracks. As shown in Figure 8, the S_0 guided wave pack does not mix with the reflected A_0 guided waves. This is because the group velocity of

the converted S_0 guided wave is much higher than that of A_0 guided wave.

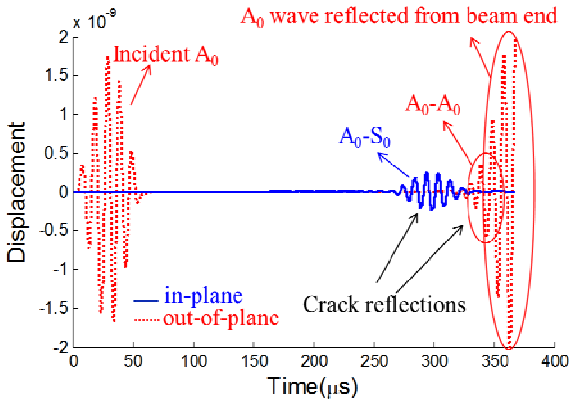

Figure 8. Displacement response measured at the beam end ($x = 0$ m) with a crack located at 0.49 m

4 PARAMETRIC STUDY

The proposed SFE model was utilised to investigate the low frequency guided wave scattering characteristics at the cracks with different depths and widths in this section. The modelled isotropic beam has length 1 m, depth 0.006 m and width 0.012 m. The crack was located at the middle of the beam. The reflected and transmitted guided wave signals were measured at $x = 0.24$ m and $x = 0.76$ m, and hence, the distances from crack to the both measurement points were 0.26 m.

Two cases were considered to study the mode conversion effect (i.e. A_0 to S_0 and S_0 to A_0, respectively). The excitation signal was a 100 kHz narrowband six-cycle sinusoidal tone burst modulated by a Hanning window, which was applied through the nodal deformation in the vertical and horizontal direction at the beam end ($x = 0$ m), to excite the A_0 and S_0 guided wave in these two cases, respectively. The wavelengths of the A_0 and S_0 waveguides at this frequency are 19.72 mm and 51.11 mm.

When the incident guided wave interacts with the crack, the reflected and transmitted waves are generated. The reflected guided wave travels back to the measurement point located at $x = 0.24$ m. For the transmitted wave, it propagates toward the measurement point located at $x = 0.76$ m. It should be noted that no baseline signal was applied to extract the amplitude of the scattered waves from the crack. In this study the measured data was normalised by the maximum absolute amplitude of displacement measured at the middle of the beam, which has the same distance to both measurement points.

One of the aims in this study is to investigate the reflected and transmitted wave amplitudes as a function of the crack size (i.e. asymmetric crack depth d_c and symmetric width b_c). Without loss of generality, the crack depth d_c and width b_c were normalised by the wavelength λ_{in} of the incident wave as

$$D_d = d_c / \lambda_{in}, \quad D_b = b_c / \lambda_{in} \tag{56}$$

where D_d and D_b are the crack depth and width to wavelength ratios, respectively.

4.1 Mode conversion from A_0 to S_0 guided wave

In this case, the A_0 guided wave was excited. Cracks with different depths were studied but the width of the cracks is a constant at the value of half of the beam width, i.e. 0.006 m. Figure 9 shows the normalised amplitude of a crack as a function of D_d while D_b equals to 0.305. It is shown that the normalised amplitude of the reflected A_0 guided wave steadily increases and reaches its local maximum at $D_d = 0.15$ where the amplitude of transmitted A_0 guided wave decreases and reaches the local minimum at around $D_d = 0.2$.

The values of D_d that having the local maximum and minimum amplitude of the reflected and transmitted A_0 guided wave are not the same. This is mainly because part of the incident energy was mode converted from A_0 to S_0 guided waves. As the value of D_d increases, the transmitted A_0 guided wave amplitude increases to reach the local maximum amplitude and then decreases again whereas the reflected wave amplitude behaves the other way around.

Figure 9 also shows that the mode converted transmitted and reflected S_0 guided waves overlap each other and the amplitude increase with the depth to crack ratio D_d. The amplitude increases almost linearly and then starts falling when D_d is around 0.22. As D_d approaching its upper considered limit, the transmitted A_0 and the mode converted S_0 guided wave amplitudes shrank sharply. At the meanwhile, the reflected A_0 guided wave amplitude increases significantly as the depth of the crack almost reaches the depth of the beam.

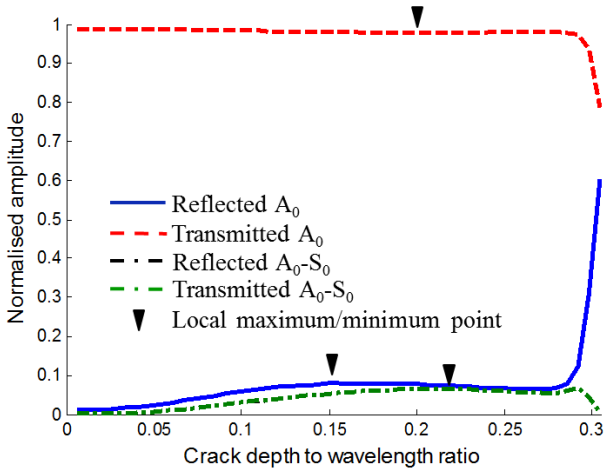

Figure 9. Normalised amplitude as a function of D_d for incident A_0 guided wave.

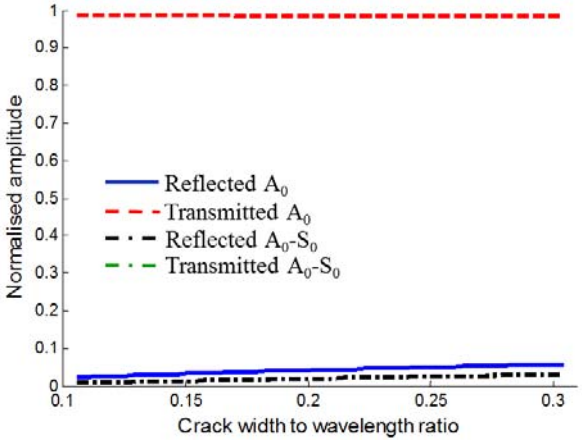

Figure 10. Normalised amplitude as a function of D_b for incident A_0 guided wave.

Figure 10 shows the normalised amplitude from a damaged beam with crack width as a variable but the depth remains unchanged at 2 mm. The normalised amplitude is thus a function of D_b and D_d is fixed at 0.101. The transmitted A_0 guided wave amplitude gradually decreases with D_b, while the reflected A_0 guided wave and the mode-converted A_0 guided wave signal gradually increases with different amplitudes. Also, the mode converted transmitted and reflected S_0 guided waves have the same amplitude. Generally, the amplitude of reflected A_0 guided wave is larger than the mode-converted S_0 guided wave.

4.2 Mode conversion from A_0 to S_0 guided wave

Different to Section 4.1, the S_0 guided wave was the incident wave in this section. The aim is to investigate the characteristics of the reflected S_0 guided wave and mode converted A_0 guided wave for different crack sizes. Figure 11 shows the normalised reflected and transmitted wave amplitude as a function of D_d with $D_b = 0.12$ (i.e. the crack width is 6 mm). Similarly, as D_d approaching the maximum value, the amplitude of the transmitted S_0 guided wave decreases but the reflected S_0 guided wave increases dramatically. They have the same amplitude at $D_d = 0.115$.

The amplitude of the mode converted A_0 guided wave increases significantly with D_d and then decreases after it reaches the maximum value at $D_d = 0.07$. The results show that the amplitudes of reflected and transmitted A_0 guided waves are identical.

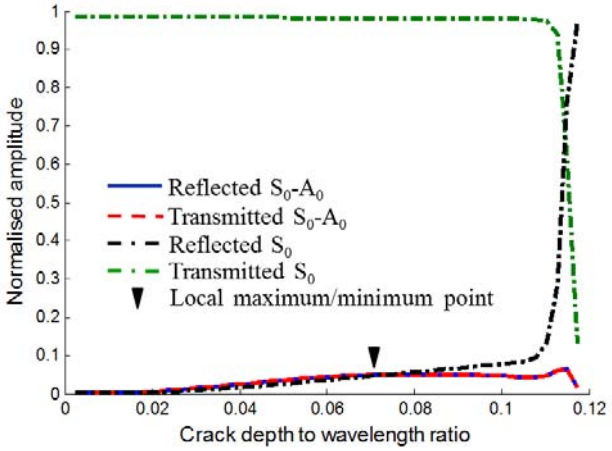

Figure 11. Normalised amplitude as a function of D_d for incident S_0 guided wave.

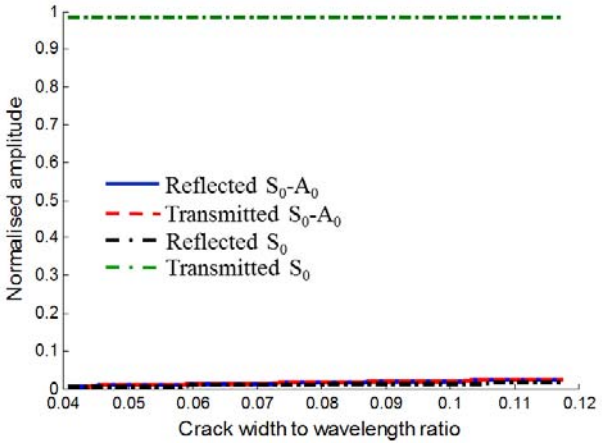

Figure 12. Normalised amplitude as a function of D_b for incident S_0 guided wave.

Figure 12 shows the normalised amplitude as a function of D_b with $D_d = 0.04$ (i.e. the depth of crack is 2 mm). It shows that the transmitted S_0 wave decreases with D_b. The amplitude of the reflected S_0 guided wave and mode-converted A_0 guided waves increase with D_b. The results show that the amplitudes of mode converted A_0 guided waves have similar values and they are larger than the reflected S_0 guided waves.

5 CONCLUSIONS

This paper studied the fundamental physical insight into the guided wave propagation in an isotropic beam using a 4-DoF SFE beam model, which was developed based on the Mindlin-Herrmann rod and Timoshenko beam theory. A spectral two-node crack element with three DoFs per node was developed to model the crack. This proposed beam model was verified using the 3D explicit FE beam model. A good agreement of the wave propagation time history was found between the results of the SFE and 3D FE methods. This study demonstrated that the proposed computational effective crack element could be used to predict the mode conversion effect between A_0 and S_0 guided waves accurately.

Parametric studies of two different damage cases were conducted to investigate the guided wave reflection and transmission characteristics at the cracks with different depths and widths. The results show that the normalised amplitudes of A_0 and S_0 guided waves were highly dependent on the crack sizes. In general, the amplitudes of reflected and mode converted guided waves increase for larger crack size except that the amplitude of the transmitted guided wave decreases. The results of the parametric studies indicate the behaviour of the normalised amplitude as a function of D_d was more complicated than that of D_b.

ACKNOWLEDGEMENTS

This work was supported by the Australian Research Council under Grant Number DE130100261. The supports are greatly appreciated.

REFERENCES

Ajith, V., and Gopalakrishnan, S. "Wave propagation in stiffened structures using spectrally formulated finite element," *European Journal of Mechanics-A/Solids,* Vol. No., 2013.

Benmeddour, F., Grondel, S., Assaad, J., and Moulin, E. "Study of the fundamental Lamb modes interaction with symmetrical notches," *NDT & E International,* Vol. 41, No. 1, 2008, pp. 1-9.

Bergamini, A., and Biondini, F. "Finite strip modeling for optimal design of prestressed folded plate structures," *Engineering Structures,* Vol. 26, No. 8, 2004, pp. 1043-1054.

Boyd, J. P. *Chebyshev and Fourier spectral methods*. 2001. Courier Dover Publications.

Carden, E. P., and Fanning, P. "Vibration based condition monitoring: a review," *Structural Health Monitoring,* Vol. 3, No. 4, 2004, pp. 355-377.

Castaings, M., Le Clezio, E., and Hosten, B. "Modal decomposition method for modeling the interaction of Lamb waves with cracks," *The Journal of the Acoustical Society of America,* Vol. 112, No. 6, 2002, pp. 2567-2582.

Chu, S. T., and Chaudhuri, S. K. "A finite-difference time-domain method for the design and analysis of guided-wave optical structures," *Lightwave Technology, Journal of,* Vol. 7, No. 12, 1989, pp. 2033-2038.

Cowper, G. "The shear coefficient in Timoshenko's beam theory," *Journal of Applied Mechanics,* Vol. No., 1966, pp. 335-340.

Darpe, A., Gupta, K., and Chawla, A. "Coupled bending, longitudinal and torsional vibrations of a cracked rotor," *Journal of Sound and Vibration,* Vol. 269, No. 1, 2004, pp. 33-60.

Deepak, B., Ganguli, R., and Gopalakrishnan, S. "Dynamics of rotating composite beams: A comparative study between CNT reinforced polymer composite beams and laminated composite beams using spectral finite elements," *International Journal of Mechanical Sciences,* Vol. No., 2012.

Delsanto, P. P., R.S., S., and Mignogna, R. B. "Connection machine simulation of ultrasonic wave propagation in materials III: The three-dimensional case," *Wave Motion,* Vol. 26, No. 4, 1997, pp. 329-339.

Delsanto, P. P., Schechter, R. S., Chaskelis, H. H., Mignogna, R. B., and Kline, R. "Connection Machine Simulation of Ultrasonic Wave Propagation in Materials 2: The Two-dimensional Case," *Wave Motion,* Vol. 20, No., 1994, pp. 295-314.

Delsanto, P. P., Whitcombe, T., Chaskelis, H. H., and Mignogna, R. B. "Connection Machine Simulation of Ultrasonic Wave Propagation in Materials I: The One-dimensional Case," *Wave Motion,* Vol. 16, No., 1992, pp. 65-80.

Doebling, S. W., Farrar, C. R., and Prime, M. B. "A summary review of vibration-based damage identification methods," *Shock and Vibration Digest,* Vol. 30, No. 2, 1998, pp. 91-105.

Doebling, S. W., Farrar, C. R., Prime, M. B., and Shevitz, D. W. Damage identification and health monitoring of structural and mechanical systems from changes in their vibration characteristics: a literature review (1996): Los Alamos National Lab., NM (United States).

Doyle, J. F. *Wave propagation in structures*. 1989. Springer.

Fan, W., and Qiao, P. "Vibration-based damage identification methods: a review and comparative study," *Structural Health Monitoring,* Vol. 10, No. 1, 2011, pp. 83-111.

He, M., and Hutchinson, J. "Surface crack subject to mixed mode loading," *Engineering Fracture Mechanics,* Vol. 65, No. 1, 2000, pp. 1-14.

Hong, M., Zhou, C., Su, Z. Q., Cheng, L., and Qing, X. L. "Nonlinear Properties of Lamb Waves under Modulation of Fatigue Damage: Finite Element Simulation with Experimental Validation," *Key Engineering Materials,* Vol. 558, No., 2013, pp. 195-204.

Kawashima, H. "The shear coefficient for quartz crystal of rectangular cross section in timoshenko's beam theory," *IEEE Transactions on Ultrasonics, Ferroelectrics, and Frequency Control,* Vol. 43, No. 3, 1996, pp. 434-440. doi: 10.1109/58.489402

Kudela, P., Krawczuk, M., and Ostachowicz, W. "Wave propagation modelling in {1D} structures using spectral finite elements," *Journal of Sound and Vibration,* Vol. 300, No. 1-2, 2007, pp. 88-100.

Kudela, P., and Ostachowicz, W. (2009). *3D time-domain spectral elments for stress wave modelling*. Paper presented

at the 7th International Conference on Modern Practice in Stress and Vibration Analysis.

Li, F., Peng, H., Sun, X., Wang, J., and Meng, G. "Wave Propagation Analysis in Composite Laminates Containing a Delamination Using a Three-Dimensional Spectral Element Method," *Mathematical Problems in Engineering,* Vol. 2012, No., 2012.

Liu, G. "A combined finite element/strip element method for analyzing elastic wave scattering by cracks and inclusions in laminates," *Computational Mechanics,* Vol. 28, No. 1, 2002, pp. 76-82.

Lowe, M. J., Cawley, P., Kao, J., and Diligent, O. "The low frequency reflection characteristics of the fundamental antisymmetric Lamb wave a0 from a rectangular notch in a plate," *The Journal of the Acoustical Society of America,* Vol. 112, No. 6, 2002, pp. 2612-2622.

Mindlin, R., and Herrmann, G. (1951). *A one-dimensional theory of compressional waves in an elastic rod.* Paper presented at the Proceedings of the 1st US National Congress of Applied Mechanics.

Moser, F., Jacobs, L. J., and Qu, J. "Modeling Elastic Wave Propagation in Waveguides with the Finite Element Method," *NDT & E Ingternational,* Vol. 32, No. 4, 1999, pp. 225-234.

Newman Jr, J., and Raju, I. "An empirical stress-intensity factor equation for the surface crack," *Engineering Fracture Mechanics,* Vol. 15, No. 1, 1981, pp. 185-192.

Ng, C. T. "Bayesian model updating approach for experimental identification of damage in beams using guided waves," *Structural Health Monitoring,* Vol. No., 2014, pp. 1475921714532990.

Ng, C. T., and Veidt, M. "Scattering of the fundamental anti-symmetric Lamb wave at delaminations in composite laminates," *The Journal of the Acoustical Society of America,* Vol. 129, No. 3, 2011, pp. 1288-1296.

Ng, C. T., Veidt, M., and Lam, H. F. "Guided Wave Damage Characterisation in Beams Utilising Probabilistic Optimisation," *Engineering Structures,* Vol. 31, No. 12, 2009, pp. 2842-2850.

Ng, C. T., Veidt, M., Rose, L., and Wang, C. H. "Analytical and finite element prediction of Lamb wave scattering at delaminations in quasi-isotropic composite laminates," *Journal of Sound and Vibration,* Vol. No., 2012.

Ostachowicz, W., Kudela, P., Krawczuk, M., and Zak, A. Spectral Finite Element Method *Guided Waves in Structures for SHM* (2012. pp. 47-92): John Wiley & Sons, Ltd.

Ostachowicz, W., and Radzieński, M. "Structural health monitoring by means of elastic wave propagation," *Journal of Physics: Conference Series,* Vol. 382, No. 1, 2012.

Pozrikidis, C. *Introduction to finite and spectral element methods using Matlab*. 2005. CRC Press.

Raghavan, A., and Cesnik, C. E. S. "Review of Guided-wave Structural Health Monitoring," *The Shock and Vibration Digest,* Vol. 39, No. 2, 2007, pp. 91-114.

Ramadas, C., Balasubramaniam, K., Joshi, M., and Krishnamurthy, C. V. "Interaction of guided Lamb waves with an asymmetrically located delamination in a laminated composite plate," *Smart Materials and Structures,* Vol. 19, No. 065009, 2010, pp. 1-11.

Reddy, J. N. *An introduction to the finite element method* (Vol. 2). 2006. McGraw-Hill New York.

Rose, J. L. *Ultrasonic Waves in Solid Media*. 1999. New York: Cambridge University Press.

Rose, J. L. "A Baseline and Vision of Ultrasonic Guided Wave Inspection Potential," *Journal of Pressure Vessel Technology,* Vol. 124, No. 3, 2002, pp. 273-282.

Rucka, M. "Experimental and numerical study on damage detection in an L-joint using guided wave propagation," *Journal of Sound and Vibration,* Vol. 329, No. 10, 2010, pp. 1760-1779.

Rucka, M., Witkowski, W., Chróścielewski, J., and Wilde, K. "Damage detection of a T-shaped panel by wave propagation analysis in the plane stress," *Archives of Civil Engineering,* Vol. 58, No. 1, 2012, pp. 3-24.

Shkerdin, G., and Glorieux, C. "Lamb mode conversion in a plate with a delamination," *The Journal of the Acoustical Society of America,* Vol. 116, No. 4, 2004, pp. 2089-2100.

Sohn, H., Farrar, C. R., Hemez, F. M., Shunk, D. D., Stinemates, D. W., Nadler, B. R., and Czarnecki, J. J. *A review of structural health monitoring literature: 1996-2001*. 2004. Los Alamos National Laboratory Los Alamos,, New Mexico.

Tada, H., Paris, P. C., Irwin, G. R., and Tada, H. *The stress analysis of cracks handbook* (Vol. 130). 2000. ASME press New York.

Veidt, M., and Ng, C. T. "Influence of stacking sequence on scattering characteristics of the fundamental anti-symmetric Lamb wave at through holes in composite laminates," *The Journal of the Acoustical Society of America,* Vol. 129, No. 3, 2011, pp. 1280-1287.

Veidt, M., and Normandin, B. "Single Transducer Pair Lamb Wave Time Reversal for Damage Detection in Composite Laminates," *Key Engineering Materials,* Vol. 558, No., 2013, pp. 205-217.

Xu, F., Zhang, Y., Hong, W., Wu, K., and Cui, T. J. "Finite-difference frequency-domain algorithm for modeling guided-wave properties of substrate integrated waveguide," *Microwave Theory and Techniques, IEEE Transactions on,* Vol. 51, No. 11, 2003, pp. 2221-2227.

Xu, K., Ta, D., Su, Z., and Wang, W. "Transmission analysis of ultrasonic Lamb mode conversion in a plate with partial-thickness notch," *Ultrasonics,* Vol. 54, No. 1, 2014, pp. 395-401.

Zhao, X. G., and Rose, J. L. "Boundary element modeling for defect characterization potential in a wave guide," *International Journal of Solids and Structures,* Vol. 40, No. 11, 2003, pp. 2645-2658.

Zhou, L., He, Z., and Sun, H. "Lamb wave mode conversion-based crack detection for plate-like structures without baseline information," *Journal of Vibroengineering,* Vol. 15, No. 2, 2013, pp. 647-657.

Zhou, W. J., and Ichchou, M. N. "Wave scattering by local defect in structural waveguide through wave finite element method," *Structural Health Monitoring,* Vol. 10, No. 4, 2011, pp. 335-349.